Research in Astronomy and Astrophysics, 23:075004 (15pp), 2023 July https://doi.org/10.1088/1674-4527/acd0e9

Mock X-Ray Observations of Hot Gas with L-Galaxies Semi-analytic Models of Galaxy Formation

Wenxin Zhong[1,2], Jian Fu[1], Shiyin Shen[1,3], and Feng Yuan[1,2]
[1] Key Laboratory for Research in Galaxies and Cosmology, Shanghai Astronomical Observatory, CAS, Shanghai 200030, China; fujian@shao.ac.cn
[2] University of Chinese Academy of Sciences, Beijing 100049, China
[3] Key Lab for Astrophysics, Shanghai 200034, China
Received 2023 February 19; revised 2023 April 12; accepted 2023 April 24; published 2023 June 9

Abstract

We create mock X-ray observations of hot gas in galaxy clusters with a new extension of the L-Galaxies semi-analytic model of galaxy formation, which includes the radial distribution of hot gas in each halo. Based on the model outputs, we first build some mock light cones, then generate mock spectra with the SOXS package and derive the mock images in the light cones. Using the mock data, we simulate mock X-ray spectra for the ROSAT all-sky survey, and compare the mock spectra with the observational results. Then, we consider the design parameters of the HUBS mission and simulate the observation of the halo hot gas for HUBS as an important application of our mock work. We find: (1) our mock data match the observations by current X-ray telescopes. (2) The survey of hot baryons in resolved clusters by HUBS is effective below redshift 0.5, and the observations of the emission lines in point-like sources at $z > 0.5$ by HUBS help us understand the hot baryons in the early universe. (3) By taking advantage of the large simulation box and flexibility in semi-analytic models, our mock X-ray observations provide the opportunity to select targets and observation strategies for forthcoming X-ray facilities.

Key words: X-rays: galaxies: clusters – galaxies: clusters: intracluster medium – galaxies: groups: general – galaxies: halos – (galaxies:) intergalactic medium

1. Introduction

According to the ΛCDM cosmological models and the results from Planck, baryonic matter contributes about 4.9% of the total mass in the universe (Planck Collaboration et al. 2020), and consists of cold baryons locked in galaxies (stars, interstellar medium (ISM), black holes, etc.; Kravtsov & Borgani 2012) and hot baryons in diffuse and ionized phases in circumgalactic medium (CGM) and intracluster medium (ICM). According to observations (Shull et al. 2012) and simulation work (e.g., Cen & Ostriker 2006), the cold baryons contribute less than 15% of the baryon budget and hot gas dominates the baryon content in the low-redshift universe.

The X-rays emitted by hot baryons can test cosmological models and provide important information on the baryon and energy cycles of galaxies and clusters, as well as trace how the dark matter structures assembled on a large scale. In the past two decades, a number of surveys by the X-ray telescopes XMM-Newton and Chandra have detected X-ray emission from hot haloes around galaxies (e.g., Li & Wang 2013; Li et al. 2017; Babyk et al. 2018). ROSAT has completed the first X-ray imaging all-sky survey in the soft X-ray band (RASS, Voges et al. 1999) and provided catalogs for thousands of galaxy clusters (e.g., Piffaretti et al. 2011; Finoguenov et al. 2020). The new X-ray telescope, eROSITA, completed the Final Equatorial-Depth Survey (eFEDS) by the end of 2019 (Brunner et al. 2022), which is a verification of the eROSITA all-sky survey (eRASS). The catalog from eFEDS, which includes 542 candidates of galaxy clusters detected as extended X-ray sources in the 140 $\deg^2$ sky area, helps in the study of CGM and ICM properties (Bahar et al. 2022; Liu et al. 2022).

A number of large-scale X-ray surveys are proposed to improve our understanding of the hot baryons in the foreseeable future. eROSITA will completes eight all-sky surveys in the soft X-ray band by the end of 2023 (eRASS:8), yielding a sample of over 10^5 galaxy clusters (Merloni et al. 2012; Predehl et al. 2021). The X-ray survey by Athena Phase B will extend the study of hot baryon distributions in ICM by mapping the properties of low-mass groups up to $z \sim 2$ (Ettori et al. 2013; Kaastra et al. 2013). The Wide Field Imager (WFI) survey, during its first four years of operation, is predicted to detect over 10,000 groups and clusters with $z > 0.5$, including 20 groups with a mass of $M_{500} \geqslant 5 \times 10^{13}\, M_{\odot}$ at around $z \sim 2$ (Zhang et al. 2020). The Chinese HUBS mission (Cui et al. 2020) intends to conduct an all-sky survey of hot baryons in warm–hot ionized medium and CGM with its large field of view and high spectral resolution (see Table 2 in Section 3.2 of this paper).

On the other hand, recent cosmological hydrodynamic simulations such as EAGLE (Crain et al. 2015; Schaye et al. 2015) and Illustris-TNG (Nelson et al. 2018; Springel et al.

2018) predict hot haloes around groups and clusters. A lot of papers study the X-ray emission from ICM and CGM using the simulation results (e.g., Stevens et al. 2017; Kovacs et al. 2019; Martizzi et al. 2019; Truong et al. 2021), and some works further make mock X-ray observations based on the plans of X-ray surveys. For example, Oppenheimer et al. (2020) makes predictions of resolved X-ray images for eROSITA with EAGLE and Illustris-TNG. Wijers & Schaye (2022) discusses the prospects for detection of X-ray emission lines for Athena X-IFU and Lynx Main Array (Gaskin et al. 2019) using EAGLE. Zhang et al. (2022) creates mock observations for HUBS with Illustris-TNG and assesses the scientific capabilities for detecting extended X-ray emission from hot gas. Vijayan et al. (2022) generates X-ray emission of ISM and CGM from MACER code (Yuan et al. 2018), and simulates HUBS observations of elliptical galaxies in four sets of simulations.

The outputs of semi-analytic models of galaxy formation (hereafter SAMs) offer another choice to build mock observations, such as the mock observatory by Overzier et al. (2013), mock cones for SKA H I Surveys by Obreschkow & Meyer (2014), and mock galaxy catalogs in multiple bands by Merson et al. (2013). Due to the low cost of running SAMs, the main advantage of their outputs is the large size of the simulation box (e.g., the box size of L-Galaxies SAMs is $500\,\mathrm{Mpc}\,h^{-1}$ based on Millennium Simulation, Henriques et al. 2015). The large simulation box helps in constructing mock observations of a very large sky area without the effect of cosmic variance even at high redshift, i.e., the $500\,\mathrm{Mpc}\,h^{-1}$ box corresponds to a sky area of over $50\,\mathrm{deg}^2$ at $z \sim 2.0$. The mock catalog based on Millennium Simulation (Springel et al. 2005) can also contain the hot gas sample in very massive haloes ($M_{200} \gtrsim 10^{15}\,M_{\odot}$). On the other hand, the flexibility of SAMs makes it possible to generate multiple mock observations based on outputs with different model parameters and prescriptions, which enables investigation of the effect of physical processes and model parameters on the observational results (Somerville & Davé 2015).

In our recent work (Zhong et al. 2023, hereafter Paper I), we develop a new extension of L-Galaxies 2015 SAMs (Henriques et al. 2015) to study the ionized hot gas in the haloes. In contrast to most previous SAMs work (e.g., L-Galaxies 2020 by Henriques et al. 2020; DARK SAGE by Stevens et al. 2016; Shark by Lagos et al. 2018), which mainly focuses on the stellar and cold gas components in galaxy disks and ISM, Paper I concentrates on the properties and spatial distribution of hot baryon components, as well as the corresponding X-ray emission from hot gaseous haloes. Our model results successfully reproduce various X-ray observations, such as the radial profiles of the temperature of hot gas, the scaling relations of X-ray luminosity, and the baryon fraction in haloes with different masses.

In this paper, we will create mock X-ray observations of the halo hot gas based on the outputs of the SAMs in Paper I. First, we will build mock light cones using the resulting spatial information, and then generate the mock spectra and images in the soft X-ray band based on some physical properties. We will consider the device parameters of X-ray facilities to mimic the observations, particularly for the HUBS mission. The mock results presented in this paper will aid in optimization of target selection and observation strategies for future X-ray surveys of hot gas, and they can also be compared to the mock results from other simulations.

This paper is organized as follows. In Section 2, we will describe the methodology used to create mock X-ray observations for hot gas in the haloes, including the steps to build mock light cones and the procedures to generate mock spectra and images. We will also show a few examples of the mock images and spectra of galaxy clusters. In Section 3, we will consider the device parameters of X-ray telescopes and simulate the observations based on the mock data. We will simulate mock spectra for ROSAT as a benchmark and then focus on the mock observations for the HUBS mission. In Section 4, we will summarize this paper and look ahead to the future work.

2. Methods

In this section, we will describe how to create the mock X-ray observations of hot gas using the model outputs of L-Galaxies SAMs. We will first describe the steps to build the mock light cones, and then the procedures to generate the mock spectra and images of galaxy clusters in the light cones. It should be noted that we do not distinguish between the definitions of galaxy "group" and "cluster" in the following sections of this paper, which denote a collection of galaxies embedded in the same dark matter halo, and we will use the term "cluster" for simplicity.

2.1. Simulation and Model Samples

The mock observations in this paper are based on the outputs of the models in Paper I, in which we developed a new branch of the L-Galaxies 2015 (Henriques et al. 2015) SAMs to describe the radial distribution of hot ionized gas in ICM and CGM. In Paper I, we use a physical model that takes into account the local instabilities and thermal equilibrium processes for hot gas in the haloes to replace the isothermal sphere in previous models. The model outputs include one-dimensional radial profiles of hot gas density, gas temperature, and the bolometric X-ray luminosity profiles around each dark matter halo. The model results successfully reproduce the X-ray observations, such as the radial profiles of hot gas density (e.g., the electron density profile from REXCESS by Croston et al. 2008 and the gas temperature profile from XMM-Newton and Chandra by Bartalucci et al. 2017), scaling relations of X-ray luminosity and temperature (Goulding et al.

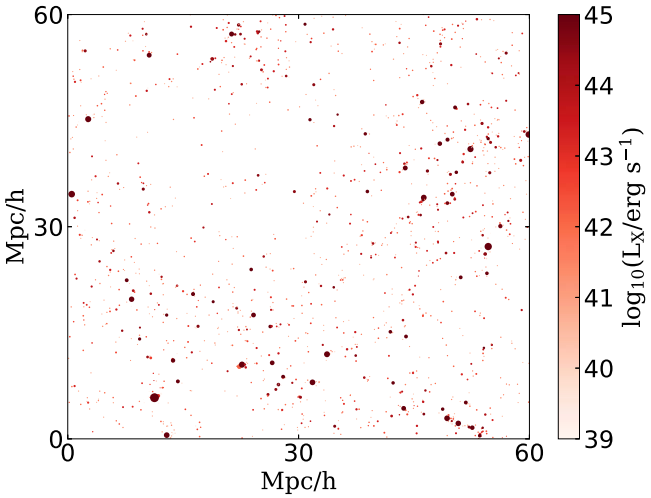

Figure 1. Illustration of the hot gas component in the model outputs in a subbox with 1/512 of the MS volume at $z = 0$ (60 Mpc h^{-1} on a side), in which each dot represents a hot gaseous halo. The size of each dot represents the halo radius R_{200} and its color represents the bolometric X-ray luminosity.

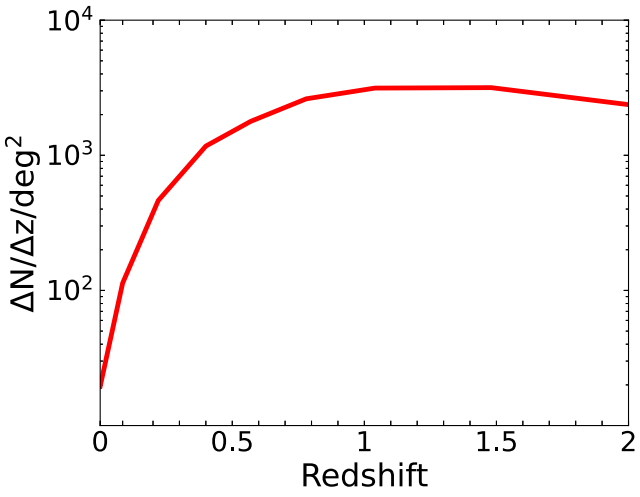

Figure 2. The redshift distribution per redshift bin ($\Delta z = 0.2$) per square degree of the haloes with $M_{200} > 10^{12}\,M_{\odot}$, averaged throughout the entire mock sky up to $z = 2$.

2016 and Babyk et al. 2018 from Chandra; Mulchaey et al. 2003 and Anderson et al. 2015 from ROSAT; Li et al. 2016 from XMM-Newton), and the baryon fraction in different haloes (Gonzalez et al. 2013 from XMM-Newton; Vikhlinin et al. 2006 and Sun et al. 2009 from Chandra).

In this paper, the SAMs results used to build the mock observations are based on the dark matter haloes of Millennium Simulation (hereafter MS, Springel et al. 2005), which is rescaled to the Planck cosmological parameters ($\Omega_{\Lambda} = 0.685$, $\Omega_m = 0.315$, $\Omega_{\rm baryon} = 0.0487$, $\sigma_8 = 0.829$, and $h = 0.673$, Planck Collaboration et al. 2020). The comoving box size of the rescaled MS (Angulo & Hilbert 2015) is about 480 Mpc h^{-1} or 713 Mpc on a side, which is several times larger than recent cosmological hydrodynamical simulations, such as EAGLE (in a box of 100 Mpc) and Illustris-TNG (in a box of 100 Mpc or 300 Mpc). The minimum halo mass is about $2.9 \times 10^{10}\,M_{\odot}$, which is the mass of 20 simulated particles. The resolution of MS is high enough to mimic the observations of the hot gas component in most galaxy clusters, and the emission from hot gas in haloes below this resolution is usually undetectable in the soft X-ray band. Based on the model results in Paper I, the gas temperature in haloes smaller than $10^{11}\,M_{\odot}$ tends to be lower than 0.1 keV.

The SAMs results are saved as halo and galaxy catalogs in a series of discrete snapshots, each of which corresponds to a certain redshift z. Based on the halo merger trees of MS rescaled to the Planck cosmological parameters, the model outputs include 59 snapshots from redshift $z \sim 56$ to $z = 0$. The catalogs include details of the spatial positions and physical properties of each halo and galaxy.

Based on the model prescriptions in Paper I, the properties of hot gas in each halo, including the gas density $\rho_{\rm hot}$ and bolometric X-ray emission profiles $L_{\rm X}$, are stored in the form of "radial profiles", which correspond to the values in a set of spherically symmetric shells with a certain radius around the halo center. To mimic the real observations, the X-ray luminosity profiles in concentric 3D shells are projected to the surface brightness in 2D rings with

$$I_{{\rm X},j} = \frac{1}{A_j}\sum_i f_{V,ij}\,L_{{\rm X},i}, \qquad (1)$$

in which $L_{{\rm X},i}$ (unit: erg s^{-1}) is the bolometric X-ray luminosity in shell i, and $I_{{\rm X},j}$ (unit: erg s^{-1} kpc^{-2}) is the projected X-ray surface luminosity in ring j. $f_{V,ij}$ represents the volume fraction of shell i projected in ring j, and A_j is the projected area of ring j. The detailed formulae and discussions on the projection can be found in papers such as McLaughlin (1999) and Ettori (2002).

In Figure 1, we show an illustration of the hot gas component in the model outputs at $z = 0$, which is one of the snapshots used to construct the light cones and mock observations. The illustration is in a subbox of the MS volume with around 60 Mpc h^{-1} on a side. In this figure, each dot represents one hot gaseous halo, and the size and the color of each dot represent the virial radius R_{200} and the bolometric X-ray luminosity of each halo.

In the framework of SAMs, we have "halo hot gas" in the model results and do not distinguish between the ionized hot gas in ICM or CGM, and we only concentrate on the X-ray emission from hot gas components inside the virial radius of each halo in this paper. We should also mention that SAMs do not consider details of the nonspherical structures such as

filaments, knots, and cosmic webs. The baryons in these structures are thought to reside in the hot gas halo or the ejecta reservoir outside the halo depending on whether they are bounded within the halo potential or not.

2.2. Light Cones

The model results of haloes and galaxies are in cubic simulation boxes at a finite number of redshifts. To mimic real observations, we convert the cubic boxes into a virtual sky using the spatial information (the 3D positions and 3D velocities). We follow the methods (MoMaF) developed by Blaizot et al. (2005) and Kitzbichler & White (2007) to create mock catalogs and light cones based on the outputs of SAMs; the details of the methods can be found in the original papers and subsequent works (e.g., Obreschkow et al. 2009; Zoldan et al. 2017). Here, we briefly describe the steps.

(i) We position the observer at the coordinate origin (0, 0, 0) and randomly replicate the simulation boxes in a 3D grid. First, we calculate the comoving distance from a box center to the observer and get the corresponding redshift, then we stack the box with the closest redshift.

Due to the relatively large size of the simulation box ($L_{\rm box} \sim 710$ Mpc for MS), it is not necessary to use the model outputs in each snapshot at the low redshift. We truncate the 3D grid at $z \sim 2$, which includes $8^3 = 512$ MS boxes. According to the forthcoming plans for X-ray telescopes, $z \sim 2$ corresponds to the redshift limit of massive cluster surveys by eRASS (Merloni et al. 2012), and also the redshift limit of the observation of warm–hot baryons and clusters by Athena (Nandra et al. 2013).

In our current work, we simply splice the boxes at different snapshots together to get a continuous cubic 3D grid and light cones, which is similar to the work by Zoldan et al. (2017) and Comparat et al. (2020). However, this simplified method may lead to discontinuities in the light cones because of the discrete redshift bins in model outputs. In some mock observation work, the authors interpolate the positions and velocities of the haloes and galaxies between snapshots (e.g., Merson et al. 2013; Smith et al. 2022), and even the intrinsic properties (stellar mass, gas mass, star formation rate, etc.) of each galaxy (Barrera et al. 2022). According to the results and discussions in Merson et al. (2013) and Smith et al. (2022), the interpolation mainly affects the results of the galaxy clustering and color assignment. In this paper, our mock observation mainly focus on the X-ray images and spectra of hot gaseous haloes, and the clustering and distribution on a large scale does not affect our mock results. On the other hand, we adopt the energy band with a continuous redshift in dealing with the mock images and spectra (see the details in Sections 2.3 and 2.4) at high redshift, which avoids producing discrete color distributions in the results.

(ii) To suppress spurious radial features caused by the repeated boxes, we assign "random tiling" on the 3D grid, which includes the random operations of shift, rotation, and inversion on the 3D coordinates and velocities.

(iii) In the stacked 3D grid, we calculate the comoving coordinates (r_x, r_y, r_z) of each object relative to the observer, and convert them to spherical coordinates (α, δ, z). The R.A. α and decl. δ are calculated as

$$\begin{aligned} \alpha &= \arctan\left(r_x/r_z\right) \\ \delta &= \arctan\left(r_y/\sqrt{r_x^2 + r_z^2}\right). \end{aligned} \tag{2}$$

Since the mock samples should have a continuous redshift distribution instead of the discrete redshift in the model outputs, we calculate the redshift z of each source with its comoving distance $d_c = (r_x^2 + r_y^2 + r_z^2)^{1/2}$ from the equation

$$d_c(z) = \frac{c}{H_0}\int_0^z \frac{dz'}{\sqrt{\Omega_\Lambda + \Omega_m(1+z')^3}}, \tag{3}$$

in which Ω_Λ and Ω_m are the cosmological parameters. The apparent redshift z_v with Doppler redshift is then calculated as

$$z_v = z_{\rm cos} + \frac{v_r}{c}(1 + z_{\rm cos}), \tag{4}$$

in which v_r is the peculiar velocity projected along the line of sight, and $z_{\rm cos}$ is the cosmological redshift in Equation (3).

(iv) Based on the model outputs in spherical coordinates mentioned above, we create light cones to mimic real observations. Considering the field of view of HUBS (1 deg^2) and eROSITA ($1\overset{\circ}{.}03 \times 1\overset{\circ}{.}03$), we choose $1^\circ \times 1^\circ$ as the angular size of each light cone. The mock data are saved according to the light cones. We generate two sets of light cones: one deep light cone and several shallow ones. The deep light cone is generated in a random direction up to $z \sim 2$. The 10 shallow light cones are generated up to $z \sim 0.2$,[4] and the center of each is a nearby cluster. Furthermore, it is quite easy to generate more light cones for further statistical analysis.

Based on the model results in Paper I, we focus on the mock data of haloes with $M_{200} > 10^{12}\,M_\odot$, since the hot gas temperature in haloes around $10^{12}\,M_\odot$ is just above 0.1 keV, and the emission from lower-mass haloes is nearly invisible in the soft X-ray band. The deep light cone up to $z \sim 2$ contains approximately 24,000 haloes above $10^{12}\,M_\odot$, and the shallow light cones up to $z \sim 0.2$ contain around 73 haloes above $10^{12}\,M_\odot$ on average. In Figure 2, we show the redshift distribution per square degree of the haloes with $M_{200} > 10^{12}\,M_\odot$, averaged throughout the entire mock sky up to redshift $z = 2$. We can see that the number of haloes per square degree peaks at $z \sim 1$ and changes little at higher redshift.

[4] We choose z up to 0.2 for the shallow light cones because the comoving distance of $z = 0.2$ is just a bit larger than the box size of MS.

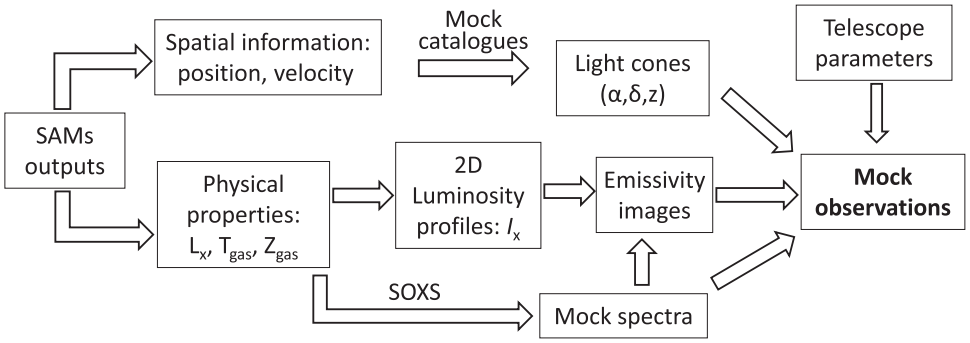

Figure 3. Brief flowchart of the steps involved in creating the mock observations in this paper.

2.3. Mock Spectra

To generate the mock spectra of the X-ray emission from the halo hot gas, we use the package "Simulated Observations of X-ray Sources" (SOXS), whose details can be found on the SOXS webpage (https://hea-www.cfa.harvard.edu/soxs). In the SOXS package, we apply the APEC spectrum generator based on hot plasmas in collisional ionization equilibrium by Foster et al. (2012) and we also consider the Galactic foreground absorption in the spectrum.

In each mock light cone, we generate a wide-band spectrum for the hot gas in each halo and also the narrow-band spectra around certain emission lines (e.g the O VII and Fe XVII lines). To generate these spectra, the following three properties from L-Galaxies model outputs are used as the input parameters for SOXS:

$L_X/4\pi d_c^2$: bolometric X-ray flux of hot gas in a halo;
T_X: luminosity-weighted mean gas temperature of a halo;
Z_{gas}: mean hot gas metallicity of a halo.

The gas metallicity Z_{gas} is defined as the metallicity in hot gas relative to the solar value,

$$Z_{gas} = \frac{1}{Z_\odot}\frac{M_{Z,hot}}{M_{hot}}, \quad (5)$$

in which $M_{Z,hot}$ is the mass of metal elements in the hot phase and M_{hot} is the mass of the hot gaseous halo. The solar metallicity $Z_\odot$ is set to be 0.02. We should note that the SAMs adopted in this paper do not contain the abundances of different elements but only one value of the total metallicity in hot gas.

For the haloes at high redshift, we make the redshift correction on the mock spectra. Considering f_o and f_e (unit: counts s^{-1} keV^{-1} cm^{-2}) as the spectra in the observed and emitted frames, the relation between f_o and f_e can be written as

$$f_o(\nu_o) = f_e(\nu_o(1+z)), \quad (6)$$

in which ν_o is the frequency in the observed frame. Then, we get the spectra in the band of the observed frame.

2.4. Mock Images

To mimic the observations, generating mock images is another important task. Using the projected surface luminosity profile in Equation (1) and the mock spectrum in Section 2.3, we obtain the mock X-ray image for each halo in the light cone.

For a nearby halo with comoving distance d_c, the emissivity S_ν (unit: erg s^{-1} cm^{-2} $arcmin^{-1}$) in a given band ν is

$$S_\nu = \frac{A_i}{4\pi d_c^2}\frac{E_\nu}{E_{bol}}I_{X,i}, \quad (7)$$

in which E_ν and E_{bol} (unit: erg s^{-1}) represent the X-ray emission energy in given band ν and the bolometric energy from the mock spectrum respectively. $I_{X,i}$ (unit: erg s^{-1} kpc^{-2}) from Equation (1) is the projected surface brightness of the bolometric luminosity in ring i of the model halo, and A_i is the projected area of ring i.

For high-redshift haloes in the deep light cone, the redshift correction is made in the calculation of the surface brightness. Similar to the K-correction in the magnitude (e.g., Hogg et al. 2002), the emissivity S_{ν_o} in a given band ν_o is

$$S_{\nu_o} = \frac{A_i}{4\pi d_c^2}\frac{E_{e,\nu_o(1+z)}}{E_{e,bol}}\frac{I_{e,X,i}}{(1+z)^4}, \quad (8)$$

in which the subscripts e and o represent the quantities in emitted frame and observed frame respectively, and the item $(1+z)^{-4}$ represents the redshift correction of the surface brightness. On the other hand, due to the cosmological redshift of the emitter, the observer can detect the X-ray emission from gas with higher temperature in high-redshift clusters, i.e.,

$$T_{gas,e} = (1+z)T_{gas,o}. \quad (9)$$

With the distribution of S_ν, we get the emissivity image for a cluster (see the examples in Section 2.5). Considering the device parameters of a specific X-ray telescope, such as ancillary response file (ARF), redistribution matrix file (RMF), point-spread function (PSF), and exposure time, we can convert the emissivity to photon-count density (unit: counts $arcmin^{-1}$)

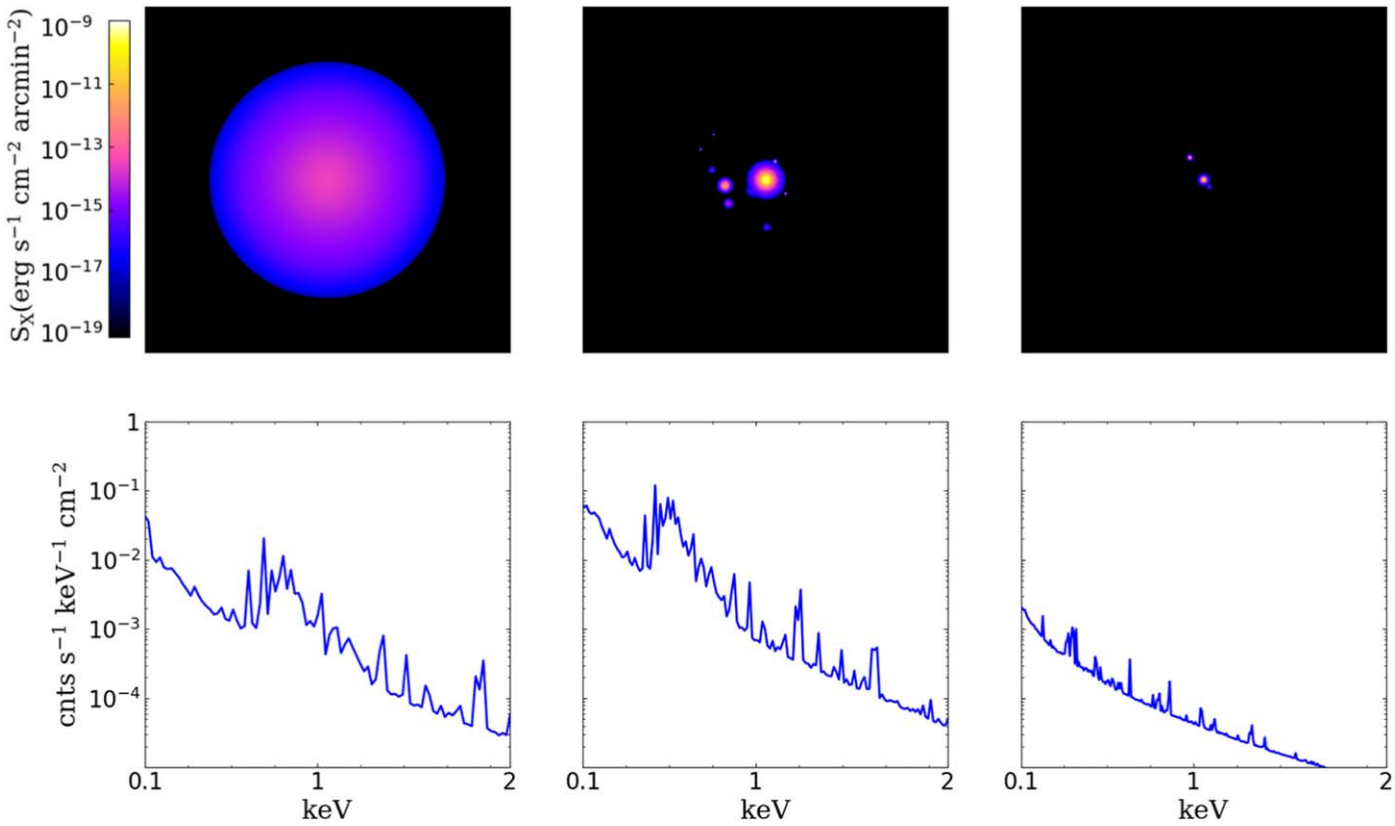

Figure 4. (Top) X-ray emissivity images in the 0.1–2 keV band with $0.^{\circ}5 \times 0.^{\circ}5$ FoV for model clusters at different redshifts. The halo masses and redshifts of the three clusters are $M_{200} = 10^{12.6}$, $10^{14.6}$, $10^{14.2}$ $M_{\odot}$ and $z = 0.03$, 0.51, 2.07 respectively. (Bottom) Mock spectra of the clusters in the top panels, generated by the SOXS package.

and generate the mock images for each cluster in the light cones (details can be found in the following sections).

In summary, we adopt the model outputs from the SAMs in Paper I to create the mock X-ray observations of the hot gaseous haloes. In Figure 3, we show a flowchart to describe the steps and procedures in this section. Here we briefly summarize the steps that we follow:

1. We adopt the L-Galaxies model outputs running on MS halo merger trees, which are stored in cubic boxes in discrete redshift bins.
2. Based on the spatial information (3D positions and velocities) of each halo, we stack the simulation boxes in a 3D grid and assign "random tiling" on the grid to suppress spurious radial features. Then we convert the Cartesian coordinates of each halo to spherical coordinates with respect to the observer.
3. We generate light cones up to different redshifts with the angular size of $1^{\circ} \times 1^{\circ}$.
4. Using the physical properties (X-ray flux, gas temperature, and gas metallicity) from the model outputs, we generate mock X-ray spectra of hot gas in each halo with SOXS packages.
5. We project the X-ray luminosity profiles in 3D shells to 2D surface brightness $I_{X,i}$ and derive the X-ray emissivity images with the mock spectra. For the haloes at high redshift, redshift corrections are made on the mock spectra and images.
6. Considering the device parameters, we simulate the observations for X-ray telescopes (see the following sections).

2.5. *Examples of Mock Images and Spectra for Clusters*

In this subsection, we will show a few mock images and spectra of hot gas in clusters at different redshifts. Considering the methods of removing contamination and identifying members of clusters by cross-matching the X-ray sources with samples from multiple wavelengths (e.g., Salvato et al. 2022), the mock images and spectra shown hereafter are based on the clusters in our mock data. We identify the members of a mock cluster through the halo merger tree in MS, i.e., all the central galaxies (Types 0 and 1) and satellite galaxies (Type 2) in the subhaloes (the substructure within the larger virialised halo) of a main friends-of-friends (FoF) halo belong to one cluster, and

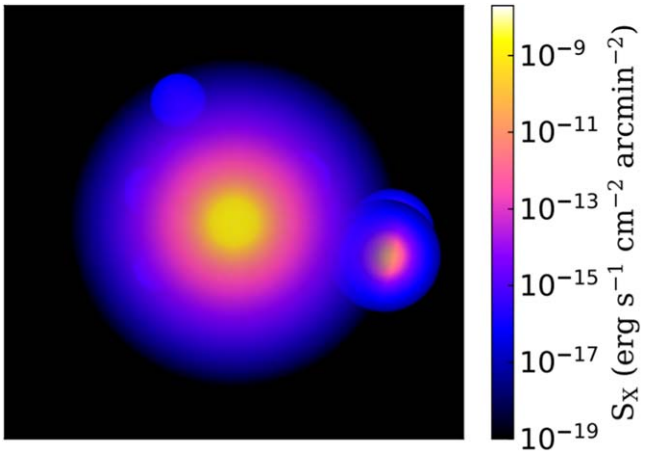

Figure 5. X-ray emissivity image in the 0.1–2 keV band of a nearby rich cluster with $M_{200} = 10^{14.7}\,M_\odot$ at $z = 0.047$; the FoV of this image is $1^\circ \times 1^\circ$. The largest source in the center represents the hot gas around the cD galaxy in the main subhalo, and other emission sources represent the hot gas around the satellite galaxies in subhaloes.

the detailed definitions of the FoF halo and subhalo can be found in Springel et al. (2005) and Croton et al. (2006). We define the central galaxy of a cluster as the galaxy in the center of an FoF halo.

To mimic the observation of the hot gas in nearby and high-redshift clusters, we show examples of mock spectra and emissivity images from three model clusters at different redshifts in Figure 4. In the left column, we select a cluster with halo mass similar to the Milky Way ($M_{200} \sim 4 \times 10^{12}\,M_\odot$ at $z \sim 0.03$) from one of the shallow light cones to mimic the observation of a nearby cluster. For the results at higher redshift, the two mock clusters are from the deep light cone. The middle column is a cluster with $M_{200} \sim 4 \times 10^{14}\,M_\odot$ at $z = 0.51$, representing a cluster close to the redshift limit of the HUBS mission for observation of extended sources (see Section 3.2 for details). In the right column, we select a cluster with $M_{200} \sim 1.6 \times 10^{14}\,M_\odot$ at $z = 2.07$, which is around the redshift limit of cluster detection for eROSITA and Athena. To show the satellite structures more clearly, we also select a cluster with $M_{200} \sim 5 \times 10^{14}\,M_\odot$ at $z \sim 0.047$ and show its emissivity image in Figure 5, which represents a nearby rich cluster with a lot of substructures and satellite galaxies around the central galaxy. In each panel of the emissivity images in Figures 4 and 5, the largest source represents the X-ray emission from the hot gas around the central galaxy and other sources are from the satellite galaxies.

The X-ray emissivity images of these clusters are in the 0.1–2 keV band, and the field of view (hereafter FoV) of the images in Figure 4 is $0.^\circ5 \times 0.^\circ5$, while that of the image in Figure 5 is $1^\circ \times 1^\circ$. We can see that all the X-ray sources are spherical because the L-Galaxies model assumes a spherically symmetrical profile for each hot gaseous halo. The outer boundary of each emission profile is located at the virial radius R_{200} of each subhalo, and the satellite beyond the outer boundary of the central galaxy belongs to another subhalo. The current version of the L-Galaxies SAMs include the hot baryons beyond the halo potential of a cluster (a.k.a. the ejected reservoir). However, the model does not consider the structure and distribution of the unbounded reservoir, so all the mock X-ray emission is from gas inside the halo boundary. Although the baryons outside the halo potential are significant, they are very difficult to probe (Walker et al. 2019; Nicastro et al. 2022), and future model work on the spatial distribution of the unbounded gas in SAMs should be meaningful (Ayromlou et al. 2022).

The emissivity images of nearby clusters in Figures 4 and 5 indicate that many X-ray facilities are capable of detecting structures like the spatial distribution of satellites, and the spatially resolved spectrum of the entire cluster. For the cluster at $z \sim 2$ in the right column of Figure 4, the angular size is around $2'$, which is around the limit of HUBS ($1.'0$ angular resolution, Cui et al. 2020), while eROSITA ($15''$ angular resolution, Merloni et al. 2012) and Athena ($5''$ angular resolution, Kaastra et al. 2013) have the ability to resolve the hot gas in the central and large satellite galaxies.

The bottom three panels of Figure 4 present the mock X-ray spectra of the clusters shown in the top panels. In each panel, we stack all the spectra from the central and satellite galaxies together to get a single spectrum for each cluster. In the left panel for the nearby cluster, we can see bumps in the 0.5–1.0 keV band in the spectrum, which are emission lines of the elements O, Fe, Ne, Mg, etc., and we will show the detail of these emission lines in the narrow-band spectra in Section 3.2. In the right panel, the relatively high gas temperature (mean $T_{\rm gas} \sim 2.5$ keV) in this massive halo leads to a high ionization fraction for some elements and weak plasma emission lines in the spectrum.

On the other hand, the high-redshift clusters extend the spectrum of the emitted frame to the band of high-energy processes, such as active galactic nuclei (AGNs) and black hole accretion. The current L-Galaxies SAMs do include the prescriptions of gas accretion and AGN feedback processes by central black holes (a.k.a. radio-mode accretion), but the X-ray emission from AGNs and black holes is not included. Some works suggest that AGN feedback affects the X-ray luminosity of haloes to some extent. Gaspari et al. (2014) shows that the action of purely AGN feedback is to lower the luminosity and heat the gas. Puchwein et al. (2008) obtains that AGN feedback significantly reduces the X-ray luminosities of poor clusters and groups. Thus, to get more accurate mock X-ray observations for high-redshift clusters, it is important to do future work on the prescriptions of the X-ray emission from black hole accretion and AGN feedback in SAMs.

Table 1
The Richness Parameter Mentioned in Dai et al. (2007), the Corresponding Bolometric X-Ray Luminosity, and the Column Density of Galactic Foreground Absorption for Each Group of the Clusters in Figure 6

Group	Richness N_{*666}	X-Ray Luminosity ($L_X/10^{42}$ erg s^{-1})	Galactic Absorption ($N_H/10^{20}$ cm^{-2})
1	0.3–1.0	0.32–0.97	0.7
2	1.0–3.0	0.97–5.57	1.4
3	3.0–10	5.57–37.7	1.8
4	10–50	37.7–484	2.8

3. Mock Observations for X-ray Telescopes

In this section, we will consider the device parameters of real X-ray facilities and simulate the observations of hot gas based on our mock data. As a benchmark, we will first simulate the X-ray spectra of the ROSAT all-sky survey and compare the mock results with the observations. Then, we will focus on the mock observations for the future HUBS mission.

3.1. Mock Spectra of Clusters for the All-sky Survey

In this subsection, we will simulate the spectra of the clusters in the first X-ray all-sky survey (RASS) by ROSAT (Voges et al. 1999) as an application of our mock spectra.

Following the procedures in Dai et al. (2007), we select clusters from the mock sky up to $z \sim 0.2$ and place them at a common distance of 100 Mpc to normalize the apparent luminosity. In Dai et al. (2007), the clusters of RASS are divided into several groups according to the optical richness, and the richness parameter N_{*666} has a fitting relation with the bolometric X-ray luminosity L_X of a cluster,

$$N_{*666} = 10^{0.43\pm0.03}\left(\frac{L_X}{10^{43}\ \mathrm{erg\ s^{-1}}\ h^{-2}}\right)^{0.63\pm0.04}. \quad (10)$$

Similarly, our mock clusters are divided into four groups based on L_X, and the parameters of each group are listed in Table 1.

Since the RASS images have already corrected the exposure times for the effects of vignetting, we use the on-axis effective area $A_{\rm eff}$ from Table 5.3 in the ROSAT handbook[5] to generate the mock spectra comparable with RASS results, then the power $F(\nu)$ (unit: counts s^{-1} keV^{-1}) received by ROSAT at frequency ν is

$$F(\nu) = f(\nu) \times A_{\rm eff}(\nu), \quad (11)$$

in which $f(\nu)$ (unit: counts s^{-1} cm^{-2} keV^{-1}) is the flux of a mock spectrum generated by the SOXS package. In addition, the Galactic foreground absorption is considered when we calculate $f(\nu)$ in Equation (11), and the column densities N_H of the foreground absorption are listed in the last column of Table 1; they are same as the values used in Dai et al. (2007).

[5] https://heasarc.gsfc.nasa.gov/docs/rosat/ruh/handbook/node122.html

Figure 6 shows the X-ray spectra in the 0.1–2 keV band derived from the mock clusters together with the observational spectra from RASS by Dai et al. (2007), and the samples are divided into four groups according to L_X and N_{*666} in Table 1. In each panel, the trough in the spectrum at around 0.5 keV is caused by the drop in the sensitivity of ROSAT between 0.3 and 0.6 keV, and the drop at $E \lesssim 0.2$ keV is caused by the foreground absorption.

As shown in Figure 6, the mock spectra can roughly match the results from RASS in the 0.1–2 keV band, and the main difference exists in Group 4 (clusters with $L_X \gtrsim 10^{43.5}$ erg s^{-1}). In these bright clusters, the flux of the mock sample at $E < 0.5$ keV is slightly higher than that of RASS, which means the model predicts lower gas temperature T_X than observations in massive haloes. For the clusters in Group 4, the average gas temperature from RASS clusters is $T_X = 4.7^{+1.4}_{-0.7}$ keV, while $T_X = 2.7$ keV for the mock sample. According to the scaling relations of the hot gas in Paper I (detailed discussions on the scaling relations of hot gas can be found in Section 3.2 of that paper), the inconsistency in the bright clusters is primarily caused by the too steep slope of the L_X–T_X relation in the mock clusters. In order to fit the relation $L_X \propto T_X^{4.5\pm0.2}$ for early-type galaxies in the range $L_X \sim 10^{38}$–10^{43} erg s^{-1} from Chandra by Babyk et al. (2018), the model result in Paper I gives $L_{X,bol} \sim T_X^{4.5}$, which is steeper than the slopes of the clusters in RASS ($L_X \propto T_X^{2.7\pm0.7}$, Dai et al. 2007) and eFEDS ($L_{X,bol} \propto T_X^{3.01}$, Bahar et al. 2022). On the other hand, according to the discussion at the end of Section 2.5, the AGN feedback suppresses the X-ray luminosity to some extent. Since the current model does not contain the X-ray emission from AGNs, it should be another cause of the discrepancy in the L_X–T_X relation in massive clusters. Future work is necessary to improve the model prescriptions in bright clusters with $L_X \gtrsim 10^{43}$ erg s^{-1}.

3.2. Mock Observations for HUBS

HUBS (The Hot Universe Baryon Surveyor) is a mission scheduled to launch around 2030 in China. Thanks to its large 1 deg^2 FoV, HUBS is at least an order of magnitude more capable than small-FoV X-ray telescopes of detecting diffuse emission from hot gas, which is thought to hide in CGM and IGM. According to the observing strategy (Cui et al. 2020), HUBS plans to observe nearby galaxies and clusters with quite long exposure times (~1 Ms), and the selection of targets is a very important task for achieving the science objects. On the other hand, the main advantages of SAMs are the large simulation box and the flexibility to investigate the effect of physical processes. In this section, we will simulate the images and the spectral observations of HUBS using our mock data of hot gas based on SAMs. This is an important application of our mock work, which may aid in optimizing future observations for HUBS mission.

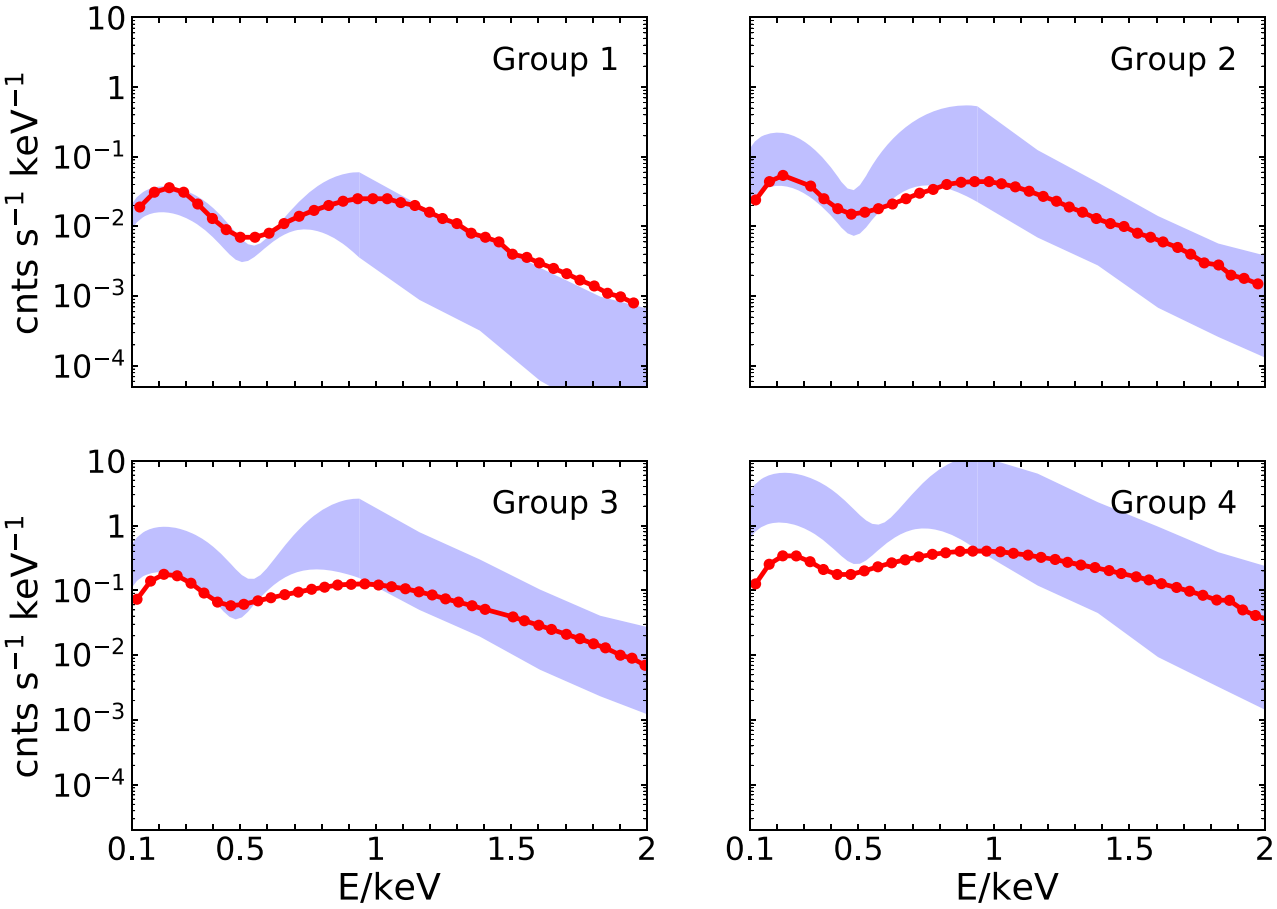

Figure 6. The comparison of the X-ray spectra from the mock clusters and the results from RASS. The mock and observational samples are divided into four panels according to the values of L_X and N_{*666} in Table 1. In each panel, the shaded area is the mock spectrum within $\pm 1\sigma$ deviation around the mean value for the mock samples, and the red curve is the average spectrum stacked from RASS data by Dai et al. (2007).

To simulate the observations of the HUBS mission, we adopt the key design parameters in Cui et al. (2020), which are shown in Table 2. It should be noted that the effective area $A_{\rm eff}$ in Table 2 is a function of energy from the ancillary response file (ARF) by Zhang et al. (2022),[6] which is used to convolve with the flux $f(\nu)$ to get the photon counts. In each light cone, we generate the wide-band and narrow-band mock spectra for each cluster, in which the wide-band spectra are in the 0.1–2 keV band with a regular energy resolution of 2 eV while the narrow-band spectra are in the bands around emission lines with a resolution of 0.6 eV. Considering the effective area, angular resolution, and exposure time of HUBS, we derive the photon-count images in both wide and narrow bands using the emissivity map and the spectra of each cluster.

In the generation of mock images and spectra, the foreground and background are also included. According to the results from XMM-Newton by Lumb et al. (2002), the cosmic unresolved X-ray background (hereafter XRB) emission is modeled with a power-law spectrum

$$S_{\rm b} = (9.03 \pm 0.24)\left(\frac{E}{\rm keV}\right)^{-1.42\pm0.03}, \quad (12)$$

in which the XRB flux density $S_{\rm b}$ is in units of counts cm^{-2} s^{-1} keV^{-1} sr^{-1}. Considering the effective area $A_{\rm eff}$ of HUBS, the background count rate can be calculated from

$$n_{\rm b} = \int S_{\rm b}(E) A_{\rm eff}(E) dE \quad (13)$$

in which $A_{\rm eff}$ is a function of energy from the ARF by Zhang et al. (2022). Then, we get the value of $n_{\rm b}$ in the 0.1–2.0 keV band:

$$n_{\rm b} = 6.3 \times 10^{-4} \text{ counts arcmin}^{-2} \text{ s}^{-1}. \quad (14)$$

For the foreground, we assume a constant column density $N_{\rm H} = 2 \times 10^{20}$ cm^{-2} (Willingale et al. 2013) for the Galactic

[6] We obtain the ARF file from Zhang et al. through private communication, and the current mock work in Section 3.2 does not include the effect of the RMF.

foreground absorption, which mainly affects the band below 0.3 keV.

In Paper I, our model results predict that the haloes between 10^{12} and $10^{13}\,M_{\odot}$ tend to contain a large fraction of hot gas with temperature below 0.5 keV, which is hard for many X-ray facilities to detect (Paerels et al. 2008). Thus, we select a nearby cluster with $M_{200}\sim 5\times 10^{12}\,M_{\odot}$ at $z\sim 0.014$ from one of the shallow light cones, and show the X-ray mock images in Figure 7. This is a typical cluster in our mock sample, representing a Local Group-sized halo in the nearby universe, which is similar to a potential target of the HUBS mission (Cui et al. 2020).

The four panels of Figure 7 show the emissivity image, wide-band image, and narrow-band images around the O VIII and Mg XI emission lines. The emissivity and wide-band images are in the 0.1–2 keV band, and the wide-band and narrow-band images are calculated with an exposure time of 10^6 s. In addition to the cluster in the center of the light cone, the images also include the emission from other sources in the 1 deg^2 FoV. We should note that all the sources in the mock images only contain the X-ray photons from hot gas, and our current SAMs outputs do not contain X-ray emission from other sources, such as AGNs and X-ray binaries.

To improve the contrast, the photons from the XRB are not shown in Figure 7. Considering the background count rate of HUBS in Equation (14), the images in Figure 7 show that HUBS is capable of detecting the X-ray emission from most of the hot gas inside the virial radius R_{200} of the nearby cluster with an exposure time of 10^6 s.

Figure 8 shows the X-ray spectra of the cluster in the center of Figure 7. To mimic the sources of contamination in the spectra, we include the contributions of all the sources in the solid angle of R_{200} to the cluster center in the light cone, and superpose the redshifted spectra from the sources of contamination onto the spectrum of the central cluster. The top panel shows the wide-band spectrum at 0.1–2 keV and the bottom panels show the zoomed-in narrow-band spectra around the emission lines of C VI, O VII, O VIII, Fe XVII, Ne X, and Mg XI. In each panel, the dashed curve shows the spectrum of the XRB, which represents the background noise in the spectrum.

With the help of the central array with high spectral resolution (0.6 eV resolution for the 12×12 small-pixel subarray in the center), Figure 8 indicates that HUBS has the ability to resolve the typical emission lines in nearby clusters, which can be used to study the properties of hot gas, such as its temperature and chemical abundances, as well as to trace the baryon cycles in the cluster environment.

Based on the mock data, we can also predict the number of the sources detectable by HUBS at different redshifts. We assume that most baryons in a cluster can be detected if the signal-to-noise ratio (S/N) is greater than 10 inside the radius R_{500} of the halo (R_{500} is the radius within which the density of a halo is 500 times the cosmic critical density at the halo's redshift). Assuming $n_{\rm s}$ and $n_{\rm b}$ are the count rates of source and background, the signal-to-noise ratio can be calculated from

$$\mathrm{S/N}=\frac{n_{\rm s}}{\sqrt{n_{\rm s}+n_{\rm b}}}. \tag{15}$$

Considering the criterion S/N > 10 and the background count rate of HUBS in Equation (14), most of the hot baryons of a cluster can be detected if the source count rate in the 0.1–2 keV band at R_{500} meets

$$n_{\rm s} > 3\times 10^{-4}\ \text{counts arcmin}^{-2}\ \text{s}^{-1}. \tag{16}$$

On the other hand, before the PSF of HUBS is finally determined, we assume that a cluster can be resolved as an extended source if it exhibits variation in the radial profile of the X-ray luminosity. Based on the 1 arcmin^2 pixel size of HUBS and the gas density profiles in the model results (see the results in Section 2.1 of Paper I and also in Sharma et al. 2012), we assume a cluster to be an extended source if the angular diameter of its R_{500} radius is greater than 3′. Clusters with smaller angular size but S/N > 10 inside R_{500} are point-like sources that HUBS cannot resolve, but it is still possible for HUBS to detect the hot baryons in these clusters with long enough exposure time.

In Figure 9, we show the redshift distribution per FoV of the clusters with S/N > 10 inside R_{500}, averaged over the entire mock sky up to $z=1$. The red curve is the number of extended sources, and the blue curve is the number of point-like sources unresolvable by HUBS. We can see that the number density of resolved clusters at $z=0$ is about 40 deg^{-2} in a redshift bin of $\Delta z=0.2$. The value peaks at $z\sim 0.4$ with almost 80 deg^{-2} per Δz and drops rapidly at $z>0.5$ for decreasing angular size. Thus, the survey of hot baryons in resolved clusters by HUBS should be effective below redshift 0.5 because of the angular size of the clusters in the soft X-ray band at different redshifts.

To test the redshift limit of resolved sources for HUBS, we select a massive bright cluster with $L_{\rm X}>10^{45}$ erg s^{-1} at $z\sim 0.5$ and show its mock observations in Figure 10. Comparing the emissivity map of the cluster in Figure 4 and the photon-count image in the left panel of Figure 10, we can see that the selected cluster is close to the angular resolution limit of HUBS. In the

Table 2
Key Design Parameters of the HUBS Mission Used to Simulate the Observations in Section 3.2

Parameter	Value
Effective area (cm^2)	0–500
Field of view (deg^2)	1.0
Spectral band (keV)	0.1–2.0
Energy resolution (eV)	
Regular	2.0
Central	0.6
Angular resolution (arcmin)	1.0

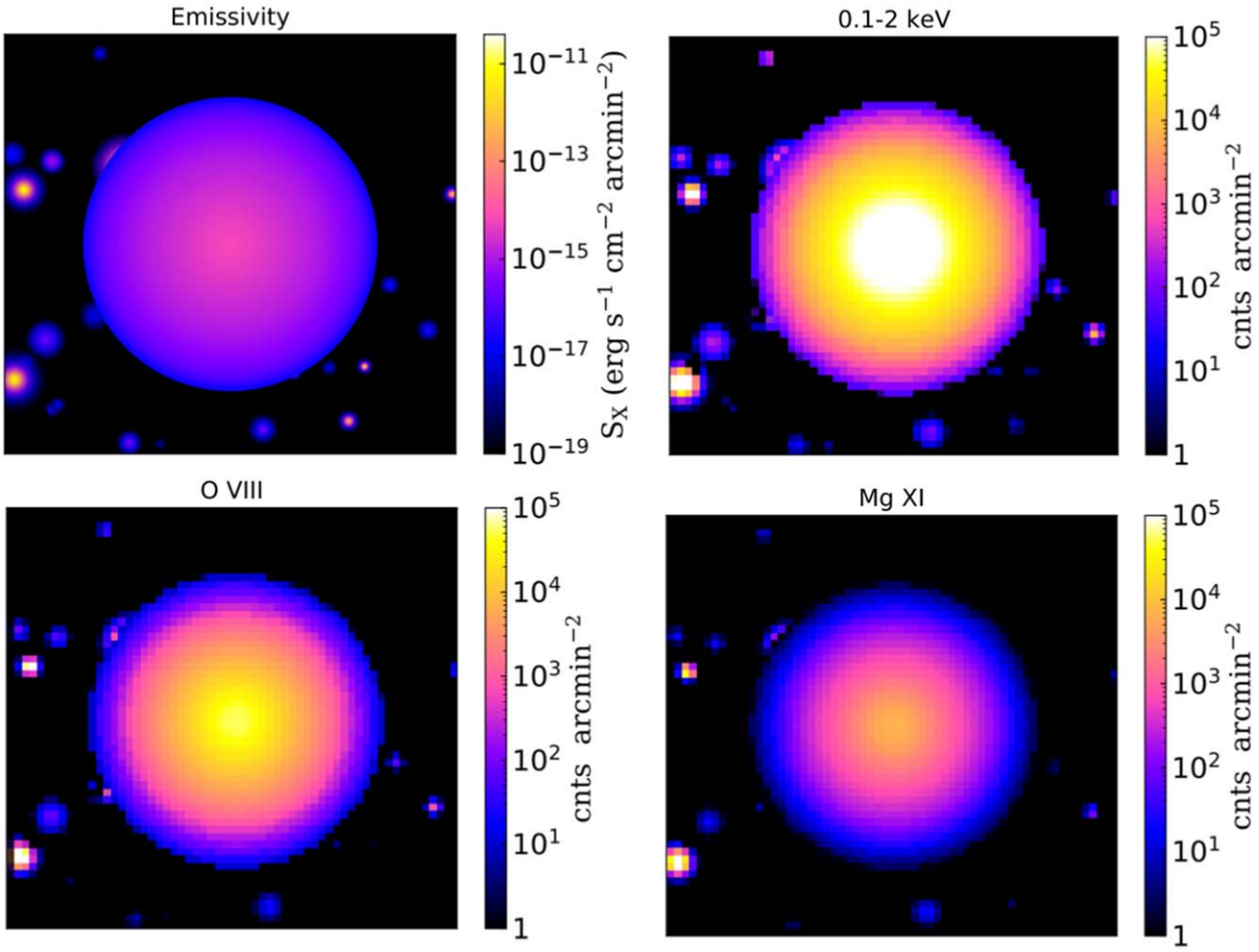

Figure 7. X-ray mock images of a light cone up to redshift 0.2 with $1^\circ \times 1^\circ$ FoV; the center of the light cone is a cluster with $M_{200} \sim 5 \times 10^{12}\, M_\odot$ at $z \sim 0.014$. The top left panel is an emissivity image in the 0.1–2 keV band. The top right panel is a mock image for HUBS in the 0.1–2 keV band with an exposure time of 10^6 s. The bottom two panels are the corresponding narrow-band images around the O VIII and Mg IX emission lines with 5 eV bandwidth. The photons from the XRB are not included in these images to improve the contrast.

middle panel of Figure 10, the S/N map indicates that the hot gas in the cluster at redshift around 0.5 can still be detected with an exposure time of 10^6 s, which is consistent with the results in Zhang et al. (2022) that HUBS can detect groups and clusters beyond $z \sim 0.3$. In addition, the mock spectrum in the right panel indicates that it is also possible for HUBS to resolve the strong emission lines in the bright cluster at $z \sim 0.5$, and the flux rate of the XRB photons is below 10^{-2} counts s^{-1} keV^{-1} (not plotted in Figure 10).

On the other hand, Figure 9 shows that the number of unresolved sources is around zero at $z = 0$ and increases with redshift. It exceeds the number of resolved clusters at $z > 0.3$ and reaches around 1000 deg^{-2} per Δz at $z > 0.8$. These unresolved sources are clusters with angular size below the angular resolution limit. Because of the large number of these point-like sources, the hot gas in these clusters contributes a significant fraction of baryons at $z \gtrsim 0.3$. It is interesting to test the mock observations of the unresolved clusters.

We select an unresolved cluster at $z \sim 1$ with high signal-to-noise ratio. The halo mass M_{200} of the cluster is around $3 \times 10^{13}\, M_\odot$, and its angular diameter of R_{500} is around $1\farcm2$. After 10^6 s of observation by HUBS, about 8×10^4 photons can be detected in the 0.1–2 keV band. The mock spectrum of this cluster is shown in Figure 11. Although the point-like source at $z \sim 1$ is below the angular resolution limit, HUBS still has the ability to detect strong emission lines from a source of this kind, such as the O VIII and Ne X lines around 0.3 and 0.5 keV in the observed frame. It should be valuable to observe some sky areas with a long

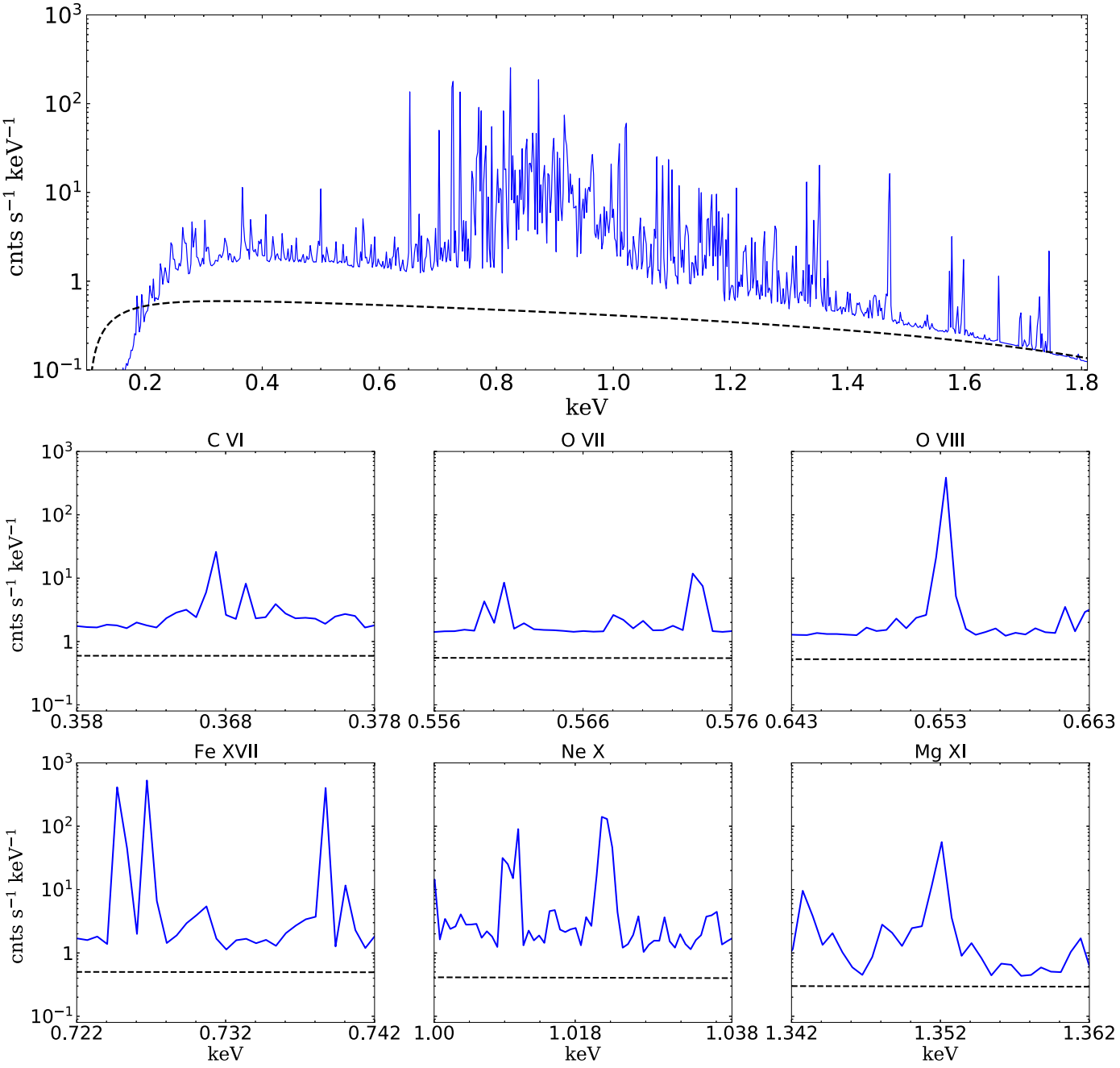

Figure 8. X-ray mock spectra of the cluster in the center of each panel in Figure 7. The top panel is the spectrum in the 0.1–2 keV band with a spectral resolution of 2 eV, and the bottom panels are the narrow-band spectra around C VI, O VII, O VIII, Fe XVII, Ne X, and Mg XI emission lines with a spectral resolution of 0.6 eV. In each panel, the dashed curve shows the spectrum of the photons from the XRB. The drop at the left end of the wide-band spectrum is caused by the Galactic foreground absorption and the decrease in effective area below the 0.3 keV band.

exposure time to get the signals from point-like sources of clusters at $z > 0.5$, which would help in studying the properties and redshift evolution of hot baryons in the early universe.

In summary, by taking advantage of the large simulation box in SAMs, the mock observation of HUBS will help in the strategies for target selection and observation for future surveys. Considering the angular size of the clusters, the survey of hot baryons in resolved clusters by HUBS is effective below redshift 0.5. HUBS has the ability to detect the emission lines of hot gas in clusters at $z > 0.5$, and the observation of

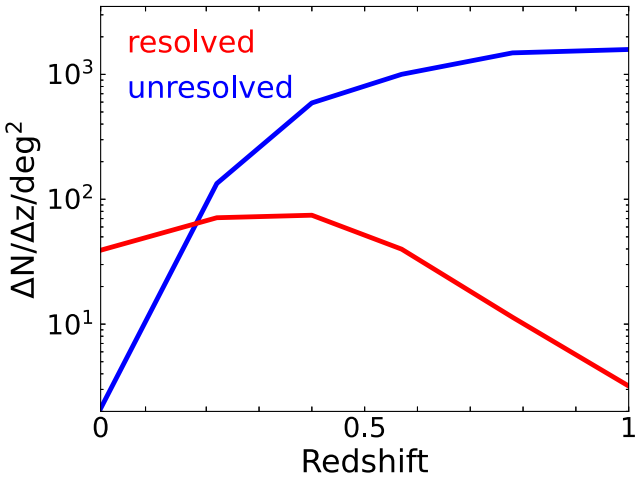

Figure 9. The redshift distribution per redshift bin ($\Delta z = 0.2$) per square degree of the clusters with S/N > 10 inside R_{500}, averaged over the entire mock sky up to $z = 1$. The red curve is the number of extended sources (angular diameter of R_{500} greater than 3′), and the blue curve is the number of point-like sources unresolvable by HUBS (angular diameter of R_{500} smaller than 3′).

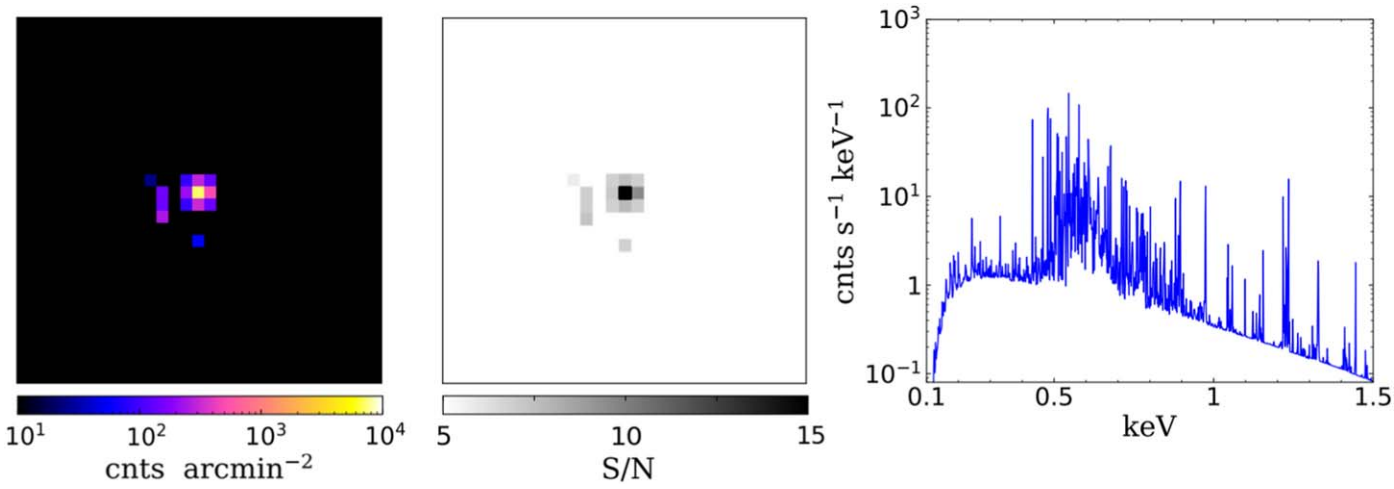

Figure 10. Mock observation of HUBS for a model cluster at $z \sim 0.5$, which is the same as the cluster in the middle column of Figure 4. The left panel is the photon-count image without the photons from the XRB, and the middle panel is the map of signal-to-noise ratio. In both panels, the exposure time is 10^6 s, and the FoV is zoomed-in to $0.^\circ5 \times 0.^\circ5$. The right panel is the mock spectrum of this cluster.

point-like sources with a long exposure time can be used to study the hot baryons in the early universe.

4. Summary

In this paper, we create mock X-ray observations of hot gas in galaxy clusters based on the model outputs of a new extension of L-Galaxies SAMs in our recent work in Paper I. First, we use the coordinates and velocities in the model outputs to build some mock light cones up to nearby and deep redshifts. In each light cone, we use the bolometric X-ray flux, gas temperature, and gas metallicity to generate mock X-ray spectra for galaxy clusters with the SOXS package, and then derive the mock X-ray images of each cluster based on the spectra and the projected X-ray luminosity profiles. Using the mock data, we simulate the X-ray spectra for the ROSAT all-sky survey and compare them with the observational results. Then, we consider the design parameters of the HUBS mission and simulate the observation of hot gas for HUBS to evaluate the results for a future survey of hot baryons, which is an important application of our mock work.

The main conclusions of this paper are:

1. Our mock X-ray observations of hot gas can approximately match the results from X-ray telescopes.
2. Due to the angular size of the clusters, the survey of hot baryons in resolved clusters by HUBS is effective below redshift 0.5. HUBS has the ability to detect the emission lines of hot gas in clusters at $z > 0.5$, and the observation

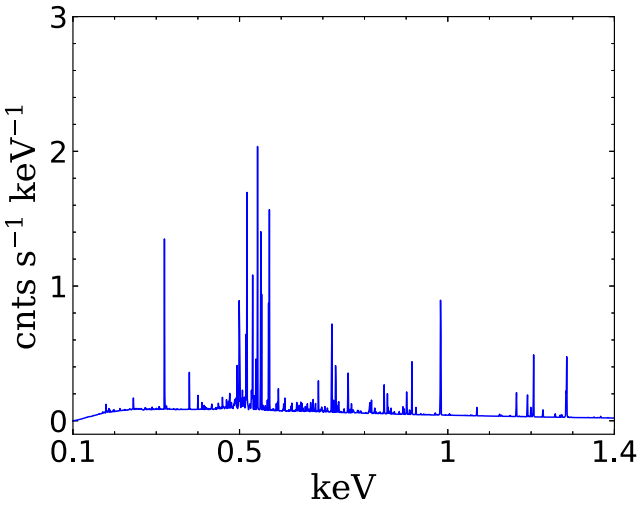

Figure 11. The mock spectrum of a cluster with $M_{200} \sim 3 \times 10^{13}\, M_{\odot}$ at $z = 1.04$. The Y-axis has a linear scale.

of point-like sources with long exposure time can be used to study the hot baryons in the early universe.

3. The mock X-ray observations provide the opportunity to select targets and optimize the observation strategies for forthcoming X-ray facilities by taking advantage of the large simulation box and flexibility in SAMs.

This paper demonstrates a few applications to use our mock data of hot gas, and many upcoming studies can be carried out in the future. One possible work is the end-to-end simulation of the all-sky hot gas survey of HUBS and eROSITA considering various systematic and instrumental effects, such as the background sources of AGNs, point-spread function, redistribution matrix file, etc., which provides the source selection and detection functions at different redshifts. Another possible work is to create mock catalogs with SAMs outputs based on ELUCID (Wang et al. 2016), a constrained N-body simulation capable of reproducing the spatial distribution of nearby galaxies and clusters in the real universe, and to simulate the X-ray observations of clusters at given positions in the real sky.

In future SAMs work, it is also necessary to improve the physical prescriptions of the hot gas and X-ray emission, including the X-ray emission from AGNs to improve the scaling relations in bright clusters, the cooling and feedback processes in inner haloes to improve the density profiles in the core regions of clusters, and also the distribution of hot baryons beyond the halo viral radius R_{200}, which is proposed to be important for the missing baryons in hydrodynamic simulations (e.g., Martizzi et al. 2019; Ayromlou et al. 2022).

Acknowledgments

The authors thank the anonymous referee for the helpful suggestions. We acknowledge the support from the National SKA Program of China No. 2020SKA0110102, the fund for key programs of Shanghai Astronomical Observatory (Grants E195121009 and E297091002), and Shanghai Committee of Science and Technology Grant No. 19ZR1466700. F.Y. is supported in part by the Natural Science Foundation of China (Grants 12133008, 12192220, and 12192223). We thank Dr. Zheng Yunliang in Shanghai Jiao Tong University for his help with the eFEDS data. We thank Prof. Cui Wei in Tsinghua University for his suggestion on carrying out the work in this paper.

ORCID iDs

Wenxin Zhong https://orcid.org/0000-0002-4299-095X
Jian Fu https://orcid.org/0000-0001-6680-0703

References

Anderson, M. E., Gaspari, M., White, S. D. M., Wang, W., & Dai, X. 2015, MNRAS, 449, 3806
Angulo, R. E., & Hilbert, S. 2015, MNRAS, 448, 364
Ayromlou, M., Nelson, D., & Pillepich, A. 2022, arXiv:2211.07659
Babyk, I. V., McNamara, B. R., Nulsen, P. E. J., et al. 2018, ApJ, 857, 32
Bahar, Y. E., Bulbul, E., Clerc, N., et al. 2022, A&A, 661, A7
Barrera, M., Springel, V., White, S., et al. 2022, arXiv:2210.10419
Bartalucci, I., Arnaud, M., Pratt, G. W., et al. 2017, A&A, 598, A61
Blaizot, J., Wadadekar, Y., Guiderdoni, B., et al. 2005, MNRAS, 360, 159
Brunner, H., Liu, T., Lamer, G., et al. 2022, A&A, 661, A1
Cen, R., & Ostriker, J. P. 2006, ApJ, 650, 560
Comparat, J., Eckert, D., Finoguenov, A., et al. 2020, JOSS, 3, 13
Crain, R. A., Schaye, J., Bower, R. G., et al. 2015, MNRAS, 450, 1937
Croston, J. H., Pratt, G. W., Böhringer, H., et al. 2008, A&A, 487, 431
Croton, D. J., Springel, V., White, S. D. M., et al. 2006, MNRAS, 365, 11
Cui, W., Bregman, J. N., Bruijn, M. P., et al. 2020, Proc. SPIE, 11444, 114442S
Dai, X., Kochanek, C. S., & Morgan, N. D. 2007, ApJ, 658, 917
Ettori, S. 2002, MNRAS, 330, 971
Ettori, S., Pratt, G. W., de Plaa, J., et al. 2013, arXiv:1306.2322
Finoguenov, A., Rykoff, E., Clerc, N., et al. 2020, A&A, 638, A114
Foster, A. R., Ji, L., Smith, R. K., & Brickhouse, N. S. 2012, ApJ, 756, 128
Gaskin, J. A., Swartz, D. A., Vikhlinin, A., et al. 2019, JATIS, 5, 021001
Gaspari, M., Brighenti, F., Temi, P., & Ettori, S. 2014, ApJL, 783, L10
Gonzalez, A. H., Sivanandam, S., Zabludoff, A. I., & Zaritsky, D. 2013, ApJ, 778, 14
Goulding, A. D., Greene, J. E., Ma, C.-P., et al. 2016, ApJ, 826, 167
Henriques, B. M. B., White, S. D. M., Thomas, P. A., et al. 2015, MNRAS, 451, 2663
Henriques, B. M. B., Yates, R. M., Fu, J., et al. 2020, MNRAS, 491, 5795
Hogg, D. W., Baldry, I. K., Blanton, M. R., & Eisenstein, D. J. 2002, arXiv: astro-ph/0210394
Kaastra, J., Finoguenov, A., Nicastro, F., et al. 2013, arXiv:1306.2324
Kitzbichler, M. G., & White, S. D. M. 2007, MNRAS, 376, 2
Kovacs, O., Bogdan, A., Smith, R., Kraft, R., & Forman, W. 2019, AAS, 233, 355.16
Kravtsov, A. V., & Borgani, S. 2012, ARAA, 50, 353
Lagos, C. del P., Tobar, R. J., Robotham, A. S. G., et al. 2018, MNRAS, 481, 3573
Li, J.-T., Bregman, J. N., Wang, Q. D., et al. 2017, ApJS, 233, 20
Li, J.-T., Bregman, J. N., Wang, Q. D., Crain, R. A., & Anderson, M. E. 2016, ApJ, 830, 134
Li, J.-T., & Wang, Q. D. 2013, MNRAS, 428, 2085
Liu, A., Bulbul, E., Ghirardini, V., et al. 2022, A&A, 661, A2
Lumb, D. H., Warwick, R. S., Page, M., & De Luca, A. 2002, A&A, 389, 93
Martizzi, D., Vogelsberger, M., Artale, M. C., et al. 2019, MNRAS, 486, 3766
McLaughlin, D. E. 1999, AJ, 117, 2398

Merloni, A., Predehl, P., Becker, W., et al. 2012, arXiv:1209.3114
Merson, A. I., Baugh, C. M., Helly, J. C., et al. 2013, MNRAS, 429, 556
Mulchaey, J. S., Davis, D. S., Mushotzky, R. F., & Burstein, D. 2003, ApJS, 145, 39
Nandra, K., Barret, D., Barcons, X., et al. 2013, arXiv:1306.2307
Nelson, D., Pillepich, A., Springel, V., et al. 2018, MNRAS, 475, 624
Nicastro, F., Fang, T., & Mathur, S. 2022, arXiv:2203.15666
Obreschkow, D., Klöckner, H.-R., Heywood, I., Levrier, F., & Rawlings, S. 2009, ApJ, 703, 1890
Obreschkow, D., & Meyer, M. 2014, arXiv:1406.0966
Oppenheimer, B. D., Bogdán, Á., Crain, R. A., et al. 2020, ApJL, 893, L24
Overzier, R., Lemson, G., Angulo, R. E., et al. 2013, MNRAS, 428, 778
Paerels, F., Kaastra, J., Ohashi, T., et al. 2008, SSRv, 134, 405
Piffaretti, R., Arnaud, M., Pratt, G. W., Pointecouteau, E., & Melin, J.-B. 2011, A&A, 534, A109
Predehl, P., Andritschke, R., Arefiev, V., et al. 2021, A&A, 647, A1
Puchwein, E., Sijacki, D., & Springel, V. 2008, ApJL, 687, L53
Planck Collaboration, Aghanim, N., Akrami, Y., et al. 2020, A&A, 641, A6
Salvato, M., Wolf, J., Dwelly, T., et al. 2022, A&A, 661, A3
Schaye, J., Crain, R. A., Bower, R. G., et al. 2015, MNRAS, 446, 521
Sharma, P., McCourt, M., Parrish, I. J., & Quataert, E. 2012, MNRAS, 427, 1219
Shull, J. M., Smith, B. D., & Danforth, C. W. 2012, ApJ, 759, 23
Smith, A., Cole, S., Grove, C., Norberg, P., & Zarrouk, P. 2022, MNRAS, 516, 4529
Somerville, R. S., & Davé, R. 2015, ARAA, 53, 51
Springel, V., Pakmor, R., Pillepich, A., et al. 2018, MNRAS, 475, 676
Springel, V., White, S. D. M., Jenkins, A., et al. 2005, Natur, 435, 629
Stevens, A. R. H., Croton, D. J., & Mutch, S. J. 2016, MNRAS, 461, 859
Stevens, A. R. H., Lagos, C. del P., Contreras, S., et al. 2017, MNRAS, 467, 2066
Sun, M., Voit, G. M., Donahue, M., et al. 2009, ApJ, 693, 1142
Truong, N., Pillepich, A., Nelson, D., Werner, N., & Hernquist, L. 2021, MNRAS, 508, 1563
Vijayan, A., Zhu, B., Li, M., Yuan, F., & Ho, L. C. 2022, arXiv:2210.12886
Vikhlinin, A., Kravtsov, A., Forman, W., et al. 2006, ApJ, 640, 691
Voges, W., Aschenbach, B., Boller, T., et al. 1999, A&A, 349, 389
Walker, S., Simionescu, A., Nagai, D., et al. 2019, SSRv, 215, 7
Wang, H., Mo, H. J., Yang, X., et al. 2016, ApJ, 831, 164
Wijers, N. A., & Schaye, J. 2022, MNRAS, 514, 5214
Willingale, R., Starling, R. L. C., Beardmore, A. P., Tanvir, N. R., & O'Brien, P. T. 2013, MNRAS, 431, 394
Yuan, F., Yoon, D., Li, Y.-P., et al. 2018, ApJ, 857, 121
Zhang, C., Ramos-Ceja, M. E., Pacaud, F., & Reiprich, T. H. 2020, A&A, 642, A17
Zhang, Y.-N., Li, C., Xu, D., & Cui, W. 2022, ExA, 53, 1053
Zhong, W., Fu, J., Sharma, P., Shen, S., & Yates, R. M. 2023, MNRAS, 519, 4344, (Paper I)
Zoldan, A., De Lucia, G., Xie, L., Fontanot, F., & Hirschmann, M. 2017, MNRAS, 465, 2236